

# Multi-wavelength observation of MAXI J1348–630 during the recent outburst using ALMA/Chandra/NuSTAR

Debasish Saha<sup>1</sup>, Sabyasachi Pal<sup>1</sup>, Manoj Mandal<sup>1</sup> and Arijit Manna<sup>1</sup>

<sup>1</sup>*Midnapore City College, Kuturia, Bhadutala, West Bengal, India 721129*

## ABSTRACT

We studied the multi-wavelength timing and spectral properties of the high mass X-ray binary MAXI J1348–630 during two successive outbursts of April and June 2019 using ALMA, Swift, Chandra, NuSTAR and NICER. The position of the source was measured by Chandra (RA=13h48m12.878s, Dec=−63°16'28.85'') with enhanced accuracy. The soft X-ray spectrum (1–6 keV) was intensively studied using Chandra/HETG from which multiple absorption-features corresponding to Fe XXII, Fe XXIII, Si XII, Cl XVI, S XV, Ar XVIII lines and the emission features corresponding to Fe XXI, Fe XXIII, Ar XVI lines were detected. We studied the first broadband spectrum for this black hole that included fluxes in radio, optical, ultraviolet and X-ray energy bands using data from ALMA (band 3, 4, 6 and 7; 89.56–351.44 GHz) and swift (UVOT and XRT). The broadband study suggested that the source was accompanied by strong blackbody radiation from the disk associated with weak synchrotron emission from the compact jets. The X-ray spectrum was also studied using NuSTAR in the range of 3–78 keV. We studied the evolution of spectral parameters using NuSTAR observations (from MJD 58655 to MJD 58672) when the source remained in the canonical hard state during the outburst of June 2019. We detected two type-C QPOs during the outburst of June 2019 with decreasing centroid frequencies from 0.82 Hz to 0.67 Hz and decreasing RMS amplitude from 7.6 per cent to 2.1 per cent. The hardness ratio showed significant variation during the outburst of April 2019 but remained almost constant during the outburst of June 2019. The spectral evolution in the hardness intensity diagram was studied during the outbursts.

*Subject headings:* X-rays: binaries – accretion, accretion discs – black hole physics – X-rays: individual: MAXI J1348–630

## 1. Introduction

Black hole transients are known to accrete matters from their companion rotational stars in the form of an accretion disk which often results in outbursts. Matters are sup-

plied to the black hole through disk winds which may generate jets. The transition between different states with a variation of timing and spectral properties are generally observed during the outburst (Homan & Belloni 2005). Black hole transients spend a large duration of time (several months to years) in quiescence, but during the time of an outburst, strong emission is observed from X-ray to radio wavelengths (Chakrabarti, Pal & Nandi 2006; Pal et al. 2006; Yusef-Zadeh et al. 2009; Cadolle et al. 2011) and the the source luminosity increases by several orders of magnitude in all wavelengths of electromagnetic spectrum (Remillard & McClintock 2006).

An outburst of a Black Hole X-ray Binary (BHXR) is characterized by its evolution through different spectral states (Remillard & McClintock 2006; Belloni 2009). BHXRBS have been observed to evolve as Hard State (HS)  $\rightarrow$  Hard-intermediate State (HIMS)  $\rightarrow$  Soft-intermediate State (SIMS)  $\rightarrow$  Soft State (SS), on the rising phase of an outburst (Homan & Belloni 2005). Energy spectra and X-ray variabilities show different characteristics on different spectral states as they evolve through the outburst. The source return to the quiescence following the reverse order of spectral states (Homan & Belloni 2005; van der Klis 2006; Belloni, Motta & Muñoz-Darias 2011; Motta et al. 2011). Most of the source evolve through the above-said spectral state sequence and create a “*q*” shaped track in the HID (Homan & Belloni 2005; Remillard & McClintock 2006; Dunn et al. 2010) during an outburst but all source does not always follow this order (Sreehari et al. 2019).

During SS, spectra are steep with typical spectral index ( $\Gamma$ )  $\gtrsim 2.5$  (Remillard & McClintock 2006). Accretion disks are relatively hotter with a typical disk temperature of  $kT \approx 1$  keV (Shakura & Sunyaev 1973; Dunn et al. 2010) and thermal X-rays are emitted from the innermost part of the accretion disk. The spectra become hard with  $\Gamma \approx 1.6$  in HS and accretion disks become relatively cooler (Makishima et al. 2008; Miller et al. 2008; Takahashi et al. 2008). Multi-wavelength observations help to understand emission mechanisms from different regions of the source, accretion phenomenon or transition through different states during the outburst of a BHXR.

BHXRBS are known to emit strong synchrotron emission from compact jets (Fender 2006; Gallo 2010). A correlation between radio and X-ray luminosities are found to be present (Gallo, Fender & Pooley 2003; Carotenuto et al. 2021) which indicates a coupling nature between the jets and the accretion disk (Yadav 2001; Corbel et al. 2003).

The BHXR transient MAXI J1348–630 was discovered during a giant outburst in January 2019 (Yatake et al. 2019). Two subsequent outbursts continued in April 2019 and June 2019 (Negoro et al. 2019). During the first outburst in January 2019, the averaged flux reached a maximum of  $\sim 4$  Crab as measured by MAXI/GSC in 2–20 keV (Tominaga et al. 2020). The second outburst of a relatively smaller magnitude started in the last week of April

2019 before the outburst of January completed its decaying phase (Negoro et al. 2019).

Previous observations suggest that the source is a black hole candidate (Sanna et al. 2019; Tominaga et al. 2020; Zhang et al. 2020). The mass of the black hole was estimated to be  $\sim 7M_{\odot}$  (Tominaga et al. 2020) and the source distance is approximately 4 kpc. From the January 2019 outburst, two low-frequency Quasi-Periodic Oscillations (QPOs) at frequency 0.57 Hz and 0.66 Hz (Jana et al. 2020) and several type-B QPOs between 4.514 Hz and 4.096 Hz were detected (Belloni et al. 2020).

In this paper, we studied the evolution of different timing and spectral properties of the black hole MAXI J1348–630 during the outburst of April and June 2019. Observation and data analysis methods of different instruments were discussed in section 2, results were summarised in section 3. The discussion and the conclusion were made in section 4 and 5 respectively.

## 2. Observations and data analysis

### 2.1. ALMA

We have used the high-resolution Atacama Large Millimeter/Submillimeter Array (ALMA)<sup>1</sup> interferometric 12 m array data for exploring the radio properties of the black hole MAXI J1348–630. The observation was done on 2 May 2019 starting from 03h07m29.7s UTC. The observational summary is given in Table 1. During the observation, the device was set up in bands 3, 4, 6, and 7 with four spectral windows. The bandwidth of all science spectral windows is 187.50 MHz which is divided into 1920 channels. The black hole was observed in ALMA band 3 to band 7 with XX, YY signal substances via integration time 1149.120 sec. During the observation, a total of 43 antennas was working with a baseline ranging from 42 to 1574 m. The antenna temperature did not exceed above 100 K because the environmental condition was very good. During the observation, the source J1427–4206 was observed as a bandpass, and flux calibrator and J1337–6503 was observed as a phase calibrator. We have used Perley-Butler 2017 (Perley & Butler 2017) for flux scale calibration.

We used the Common Astronomy Software Application (CASA v 5.4.1)<sup>2</sup> for initial data reduction and continuum imaging of black hole MAXI J1348–630 with standard calibration scripts. After calibration, we used the task `MSTRANSFORM` to split the corrected target data

---

<sup>1</sup><https://www.almaobservatory.org/en/home/>

<sup>2</sup><https://casa.nrao.edu/>

set and the continuum image of the source was made by using task `TCLEAN` with the stokes I parameter. The image was deconvolved several times with 12000 iterations. We also used the task `UVCONTSUB` for background noise subtraction and several self-calibration processes. The self-calibration process was done by the tasks `GAINCAL` and `APPLYCAL`.

## 2.2. Chandra

The Chandra observatory uses mirrors with multiple instruments to focus and collect X-rays from highly energetic celestial objects. The focal plane consists of two science instruments – Advanced CCD Imaging Spectrometer (ACIS) and High-Resolution Camera (HRC) which captures the high-resolution images created by mirrors and collects information about incoming X-rays. There are two other science instruments onboard Chandra for high-resolution spectroscopy – High Energy Transmission Grating (HETG) ([Canizares et al. 2005](#)) and Low Energy Transmission Grating (LETG) ([Brinkman et al. 2000](#)) spectrometers. Science instruments onboard Chandra have the capabilities to collect and analyze X-ray images and properties of celestial bodies with exceptional accuracy having an angular resolution of 0.5" over the energy range of 0.2–10 keV.

The Chandra observation of the black hole binary MAXI J1348–630 was made using ACIS array during the outburst with HETG (Obs Id – 21239). The observation log is summarised in Table 1. We have analysed these data using `CIAO v 4.12` with the latest `CALDB v 4.9.4`. We followed the standard Chandra data analysis threads for data reduction and analysis. The task `tgdetect2` was used to find the location of the source from the zero-order image and the location of High Energy Grating (HEG) and Medium Energy Grating (MEG) were found using the tool `tg_create_mask` from the level 1 data products. The tool `tg_resolve_events` was used to assign the grating events and necessary filters were applied using `dmcopy` to create the level 2 event files. The standard PHA files were extracted using the tool `tgextract` from the level 2 event file. This task created spectra of different orders (i.e.,  $\pm 1$ ,  $\pm 2$  and  $\pm 3$ ) from both HEG and MEG. Necessary Response Matrix Files (RMFs) and Ancillary Response Files (ARFs) were produced using the tasks `mkgrmf` and `fullgarf`. Chandra localization of the source was performed using the task `wavdetect`.

## 2.3. NuSTAR

The Nuclear Spectroscopic Telescope Array (NuSTAR) is a space-based X-ray satellite that operates in the energy range of 3–79 keV. It has two detector units – FPMA and FPMB

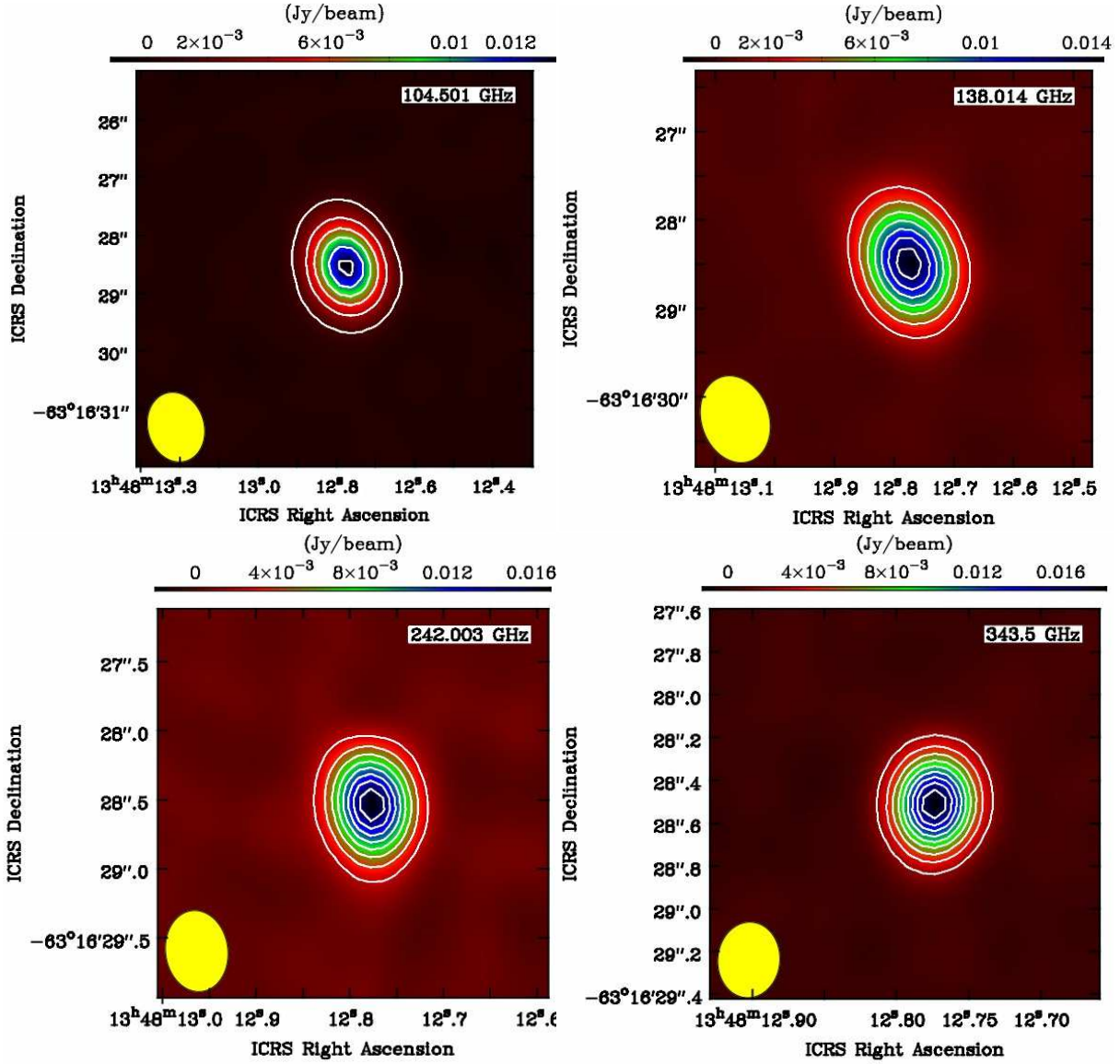


Fig. 1.— ALMA continuum image of black hole MAXI J1348–630 obtained on 2019 May 2 at 104.501 GHz, 138.014 GHz, 242.003 GHz and 343.500 GHz frequencies and computed using natural weight. The synthesized beams for observations with each frequency are shown in one corner of each images. The relative contour levels are 2, 4, 6, 8, 10, 12, 14, 16, 18 mJy.

(Focal Plane Modules – A and B) each located at the focus of two co-aligned optics units. Each detector unit is comprised of four segments made of Cadmium Zinc Telluride (CdZnTe or CZT) having a rectangular shape of dimension  $20\text{mm} \times 20\text{mm} \times 2\text{mm}$ , gridded into  $32 \times 32$  pixels. Each detector has angular resolutions of  $58''$  Half Power Diameter (HPD) and  $18''$  Full-width at Half-Maximum (FWHM). Energy resolution of each telescope is 0.4 keV at 6 keV and 0.9 keV at 60 keV respectively with  $13' \times 13'$  field of view (Harrison et al. 2013).

NuSTAR performed three observations towards MAXI J1348–630 during the HS of the outburst for 13.8 ks, 15.4 ks and 17.2 ks exposure time (Obs Ids – 80502304002, 80502304004 and 80502304006 respectively). Summary of the NuSTAR observation is given in Table 1. NUPipeline tool was used to produce the level 2 data from which we have extracted light curves, images and spectra using the tool NUPRODUCTS provided by NUSTARDAS package. Data processing has been done using HEASOFT v 6.25 software with the recent version of the calibration database.

Interday variation of the spectral parameters of the source during the decaying phase of the outburst was studied using NuSTAR data. Spectra were plotted and models were fitted using XSPEC v 12.10.1 (Arnaud 1996). Spectra were plotted in the energy range 3–78 keV, because outside this range photon statistics were not very significant. We tried different models to fit the spectra that were discussed in the result section. The summary of fitted spectral parameters is given in Table 4.

## 2.4. NICER

The Neutron star Interior Composition Explorer (NICER) on the International Space Station (ISS) is dedicated mainly to study neutron stars. The primary instrument of NICER

Table 1: Log of ALMA, Chandra, NuSTAR, NICER and Swift observations

Instrument	Observation Id	Band/Filter	Date	Start Time	MJD	Exposure (ks)
ALMA	2018.1.01034.T	Band-3 (89.56–105.43 GHz)	2019-05-02	04:15:00	58605.18	1.104
	2018.1.01034.T	Band-4 (137.06–152.93 GHz)	2019-05-02	04:34:00	58605.19	1.150
	2018.1.01034.T	Band-6 (223.07–105.43 GHz)	2019-05-02	03:50:00	58605.16	1.279
	2018.1.01034.T	Band-7 (335.56–351.44 GHz)	2019-05-02	03:06:00	58605.13	2.670
Chandra	21239	–	2019-06-21	10:59:15	58655.45	19.120
NuSTAR	80502304002	–	2019-06-21	09:21:09	58655.38	13.784
	80502304004	–	2019-06-26	11:46:09	58660.49	15.368
	80502304006	–	2019-07-08	08:46:09	58672.36	17.183
NICER	2200530160	–	2019-06-20	11:37:57	58654.48	2.162
	00011107032	–	2019-05-03	09:25:35	58606.39	0.534 (XRT)
	Swift	uvm2 ( $\lambda = 2246 \text{ \AA}$ )				0.526 (UVOT)
Swift	00011107033	uvw2 ( $\lambda = 1928 \text{ \AA}$ )	2019-05-06	11:14:36	58609.47	0.857 (UVOT)
	00011107034	u ( $\lambda = 3465 \text{ \AA}$ )	2019-05-09	10:22:35	58612.43	0.958 (UVOT)

is the X-ray Timing Instrument (XTI) which is an array of 56 X-ray photon detectors that collect photons in the energy range 0.2–12 keV (Gendreau et al. 2016). After the discovery of MAXI J1348–630, NICER performed multiple observations towards the source. We used the observation of 20 June 2019 (Obs Id – 2200530160) for the study of the power spectral properties of the source. We performed NICERL2 to apply the standard NICER calibrations and standard screening. We have applied barycenter correction by performing BARYCORR using ICRS as the reference frame. Light curves have been extracted using the barycenter corrected event file in XSELECT v 2.4e with different bin sizes of 1 sec, 0.1 sec, 0.01 sec etc.

## 2.5. Swift

The Neil Gehrels Swift Observatory is a multi-wavelength observatory that operates in a wide range of energies including optical, ultraviolet, X-ray and gamma-ray wavebands by three different instruments onboard it. The Burst Alert Telescope (BAT) operates in the energy range of 15 to 150 keV which detects any event and the corresponding location in the sky (Barthelmy et al. 2005). BAT use to monitor the whole sky regularly. We used daily monitoring data of Swift/BAT (15–50 keV) to plot the light curve (Figure 2) and HID (Figure 5).

The X-ray Telescope (XRT) onboard Swift operates in the energy range 0.3 to 10 keV to study different spectral properties of the source (Burrows et al. 2000). Since the resolution of XRT is better than that of BAT, it is often used to determine the location of any source with higher accuracy. We performed XRTPipeline using the level 1 event files and image files from the archived data to produce re-calibrated cleaned level 2 data products. We selected a source region and a background region using the imaging tool DS9. Using these calibrated, screened event files and regions files, we extracted high-level products (i.e. light curves, spectra and image files) from the task XRTPRODUCTS. The XRT spectrum in the energy range 0.9–9 keV was included in the broadband spectrum of Figure 10.

Ultraviolet/Optical Telescope (UVOT) operates in both UV and visible regions with six different filters in it (1928–5468 Å) (Poole et al. 2008). We used three different UVOT observations performed on MJD 58606, MJD 58609 and MJD 58612 for the study of broadband spectrum. Observation logs and a list of filters used during the observations were shown in Table 1. We checked if the UVOT image files were aspect corrected or not using the task FKEYPRINT. Since the correction was previously performed, we run UVOTDETECT for the source location on the UVOT sky image. We choose the source region to be a circle of radius 10'' around the source and the background region having an annulus shape with an inner and outer radius of 20'' and 30'' respectively keeping the source at the centre for each

observation. We performed the routine `UVOTSOURCE` to examine the photometry of the source keeping the background threshold  $5\sigma$ . The results were used in the broadband spectrum in Figure 10.

We have used the monitoring data of Swift/BAT (15–50 keV) and MAXI/GSC (2–20 keV) to study the temporal variation of flux during the outbursts. To study the hardness evolution, we have used MAXI/GSC data in the energy ranges 2–6 keV and 6–20 keV. We studied the Power Density Spectrum (PDS) of the source using the tool `POWSPEC` over different phases of the outburst. To find the presence of QPOs, we have analysed different observations of Swift, NuSTAR and NICER data during different phases of two outbursts. PDS is studied using the task `POWSPEC` for different bin sizes like 10 sec, 1 sec, 0.1 sec and 0.01 sec. We used the `LCMATH` tool for the background correction. The hardness intensity diagram was plotted using MAXI/GSC hardness (6–20 keV/2–6 keV) and Swift/BAT flux (15–50 keV).

### 3. Results

#### 3.1. Chandra and NuSTAR localization

On 26 January 2019, the new X-ray transient MAXI J1348–630 was discovered by MAXI/GSC and the measured position of the source was RA=13h48m12s, Dec=−63°04'04" (J2000) with 90 per cent C.L. elliptical error region having semi-major and semi-minor axes of 0.42° and 0.34° respectively (Yatake et al. 2019). Later, Denisenko et al. (2019) found the optical counterpart of MAXI J1348–630 using the iTelescope.Net T31 instrument and determined the position of the source as RA=13h48m12.88s, Dec=−63°16'28.4" (J2000). Using an 1 ks Target of Opportunity (ToO) observation with Swift, Kennea & Negoro (2019) found a bright source located at RA=13h48m12.73s, Dec=−63°16'26.8" (J2000) with 1.7" error radius (90 per cent confidence).

Chandra observed the black hole MAXI J1348–630 on 21 June 2019 with 19 ks exposure. Analysis of Chandra data revealed a bright point source located at RA=13h48m12.883s, Dec=−63°16'28.82" (J2000) with an error circle of 0.5" (90 per cent confidence). The position of the source measured by Chandra was about 2.16" away from the position measured by Swift/XRT. The position of the source found from the optical counterpart lies only 0.36" away from the Chandra measured position.

### 3.2. Temporal variations of X-ray emission

The Burst Alert Telescope (BAT) on board Swift<sup>3</sup> and Gas Slit Camera (GSC) onboard MAXI<sup>4</sup> are continuously monitoring the source from its discovery. Two subsequent outbursts occurred in April and June 2019 after the giant outburst in January 2019 (when the source was discovered). In this study, we have focused on the later two outbursts (i.e., the outburst of April and June 2019) that occurred between MJD 58596 and MJD 58709, covering approximately 113 days. Light curves using daily monitoring data of Swift/BAT and MAXI/GSC is shown in Figure 2. Variation of flux from the source observed by MAXI/GSC in 2–20 keV is shown in the upper panel (in red) and that using Swift/BAT in 15–50 keV is shown in the lower panel (in blue).

The April 2019 outburst of a relatively smaller magnitude (compared to the outburst of January) started at the end of April 2019 (MJD 58596) and continued for almost 17 days before the decaying phase of the giant outburst of January reached its quiescent level. The flux reached the peak value  $0.32 \pm 0.01$  Crab on MJD 58604 as measured by Swift/BAT (15–50 keV) and  $0.211 \pm 0.005$  Crab on MJD 58601.5 as measured by MAXI/GSC (2–20 keV). The outburst observed in 15–50 keV by Swift/BAT was comparatively more prominent than that observed in 2–20 keV by MAXI/GSC.

The next outburst (outburst of June 2019) with a relatively larger magnitude compared to that of April was started in June 2019 (MJD 58630 approx) as observed by Swift/BAT. The outburst continued for almost 70 days and during the outburst, the flux reached the peak ( $0.83 \pm 0.03$  Crab) on MJD 58653 as observed by Swift/BAT in the energy range of 15–50 keV. The peak flux measured by MAXI/GSC in 2–20 keV was  $0.35 \pm 0.07$  Crab on MJD 58654.5.

The source showed the variability of different time scales. Many micro-flaring activities were detected. In Figure 3, we have shown an example of a micro-flare of  $\sim 15$  s duration that has been detected using NuSTAR data (Obs Id – 80502304002) on MJD 58655. The source shows a sharp rise and relatively slow decay, which is the typical nature of a micro-flare. It took  $\sim 5$  sec to reach from  $212 \text{ count s}^{-1}$  to  $486 \text{ count s}^{-1}$  and  $\sim 10$  sec to come back to the base value.

---

<sup>3</sup><https://swift.gsfc.nasa.gov/results/transients/>

<sup>4</sup><http://maxi.riken.jp/top/index.html>

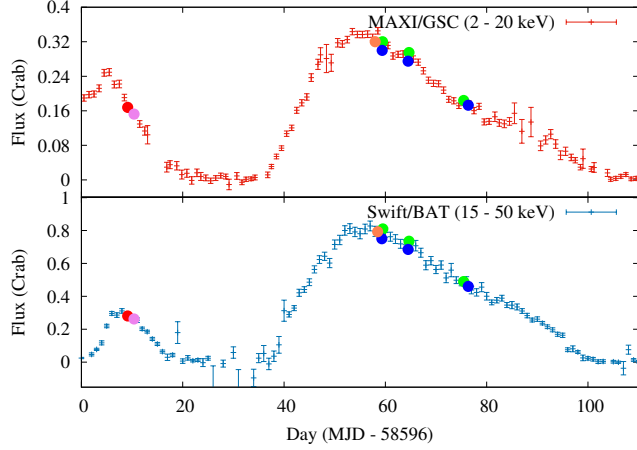


Fig. 2.— Variation of flux towards the source MAXI J1348–630 during the outbursts of April and June 2019 using Swift/BAT and MAXI/GSC. In the upper panel, the variation of the flux using MAXI/GSC (in red) in the energy range 2–20 keV is shown while in the lower panel the variation of the flux in 15–50 keV of Swift/BAT is shown (in blue). The nature of the variation of flux during two successive outbursts in different energy ranges is observed. Each circle in the plot indicates the time of observations of different instruments over different phases of the outburst. Red and violet circles denote ALMA and Swift observations respectively, while orange, green and blue circles are to indicate NICER, Chandra and NuSTAR observations respectively.

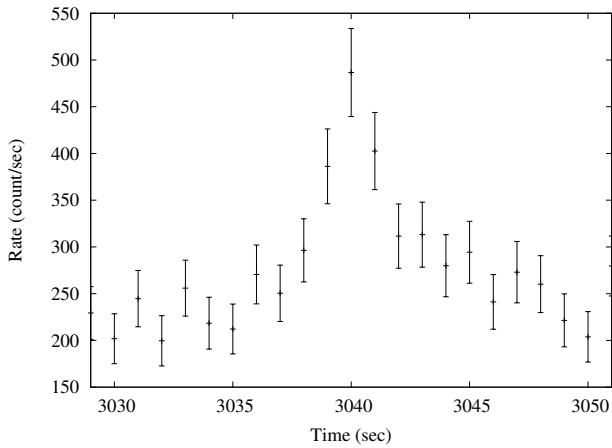


Fig. 3.— Several micro-flares are detected during the course of two outbursts. The figure shows example of a micro-flare of  $\sim 15$  s that has been detected using NuSTAR data on MJD 58655 (Obs Id – 80502304002).

### 3.3. Hardness evolution

The Hardness Ratio (HR) of the source during two successive outbursts of April and June were shown in Figure 4 where HR for two outbursts were plotted in different panels. In both figures, the upper and the middle panel showed the variations of fluxes in the energy range 2–6 keV and 6–20 keV of MAXI/GSC respectively. Each point on these two plots represented the one day averaged count rate. The bottom panels showed the evolution of hardness (6–20 keV/2–6 keV) during the outbursts which indicated the transitions of the source through different spectral states.

The left side figure showed the variations of flux and hardness that have been plotted over 30 days (from MJD 58590 to MJD 58620) during the outburst of April. The source rose and decayed in 6–20 keV but was in the declining phase, continuing the earlier outburst of January 2019 in 2–6 keV. Initially, the source was observed to remain in the SS before the initiation of the outburst, but during the outburst, the source made a transition to the HS.

In the right-side figure, the variation of flux in the energy ranges 2–6 keV and 6–20 keV and their hardness evolution were plotted for 90 days (from MJD 58620 to MJD 58710) during the June 2019 outburst using MAXI/GSC data. Variation of flux was observed in both soft and hard energy bands.

HID for the outburst of April 2019 was shown in Figure 5. The hardness ratio (6–20 keV/2–6 keV) was plotted using MAXI/GSC data while the flux was measured by Swift/BAT in 15–50 keV. In the HID, the spectral state transitions of the black hole MAXI J1348–630 were shown during the outburst of April (from MJD 58596 to MJD 58614). Earlier, the source made a transition from HS to SS during the outburst of January 2019 after its discovery (Tominaga et al. 2020; Zhang et al. 2020). It remained in the SS until MJD 58597 and the second outburst happened (outburst of April 2019) and it started to make a transition from SS to HS. At the end of the second outburst (on MJD 58608), it completely reached HS and returned to quiescence. The track shown in the HID indicated these state transitions during the April 2019 outburst.

### 3.4. Power Density Spectra

The evolution of power spectral properties was studied during two outbursts. We studied the PDS using the archival data of Swift, NuSTAR and NICER to investigate the possible presence of QPOs during this period. We detected a low-frequency QPO at 0.82 Hz from NICER observation (Obs Id – 2200530160) on MJD 58654 with a bin size of 0.1 sec. The observation was made during the outburst of June when the source was in the HS. In Figure

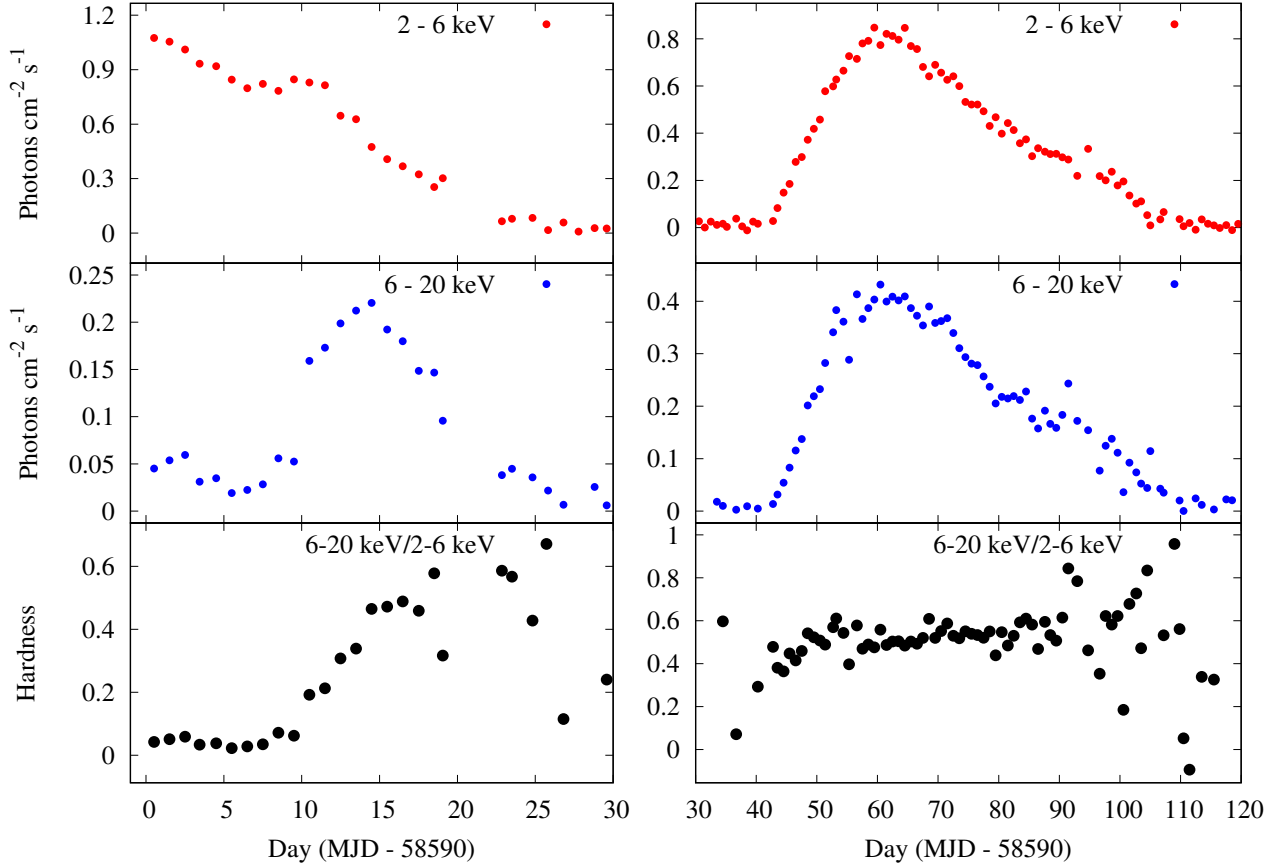


Fig. 4.— Evolution of flux during the two consecutive outbursts at different energy bands as well as the variation of hardness using MAXI/GSC data are shown. In both plots, the upper and the middle panels show the variations of flux towards the source in the energy ranges 2–6 keV and 6–20 keV respectively. The bottom panel shows the evolution of hardness (6–20 keV/2–6 keV) of the photons during the outburst. In the left figure, the flux is negligible for soft photons whereas that for hard photons is comparatively much prominent. Variation of hardness from soft to hard is also detected indicating a state transition. In the right figure, the fluxes in the different energy ranges are comparatively stronger than those in the previous one. The outburst was equally dominated by the soft and hard photons. No evidence of state transition is observed from the hardness ratio plot during the outburst of June 2019.

6, the fitted PDS of the source using NICER observation was shown. The PDS is well fitted with a combined model of constant, power-law and a Lorentzian. The fitted model gave the RMS value of 7.6 per cent and Q-value ( $\nu/FWHM$ ) = 6.83. We detected another QPO at 0.67 Hz using NuSTAR data (Obs Id – 80502304002) on MJD 58655 with an RMS value of 2.1 per cent and a Q-value of 5.58.

The centroid frequencies of QPOs decreased from 0.82 Hz to 0.67 Hz and the RMS dropped from 7.6 per cent to 2.1 per cent on a time scale of 1 day. The change in RMS is because the PDS is studied in two different energy ranges of NICER (0.2–12 keV) and NuSTAR (3–80 keV). NICER measured counts of soft photons, whereas NuSTAR measured that for hard photons. The source remained in the HS during these two observations. For this reason, the average count rate of hard photons was higher than that of soft photons. RMS of a QPO is inversely proportional to the square root of the mean count rate. Because of all these reasons, the RMS measured by NuSTAR was less than that measured by NICER.

### 3.5. Study of Chandra grating spectrum

We studied the high-resolution Chandra/HETG spectrum using the HEG-1 product. For this study, we used data of 21 June 2019 (Obs Id – 21239) near the peak of the outburst of June 2019. Multiple emission and absorption features were present in the spectrum. For this reason, we divided the whole spectrum into two different energy ranges to study them properly. The first spectrum was plotted in 1–2 keV and the other was plotted in the energy range of 2.3–6 keV. Absorption lines of high significance were observed in both spectra.

The spectrum in the energy range 1–2 keV was shown in the left of Figure 7. The spectrum was fitted with the model `phabs`, accounting for the photoelectric absorption, along with a power-law. Three absorption lines were visible in the spectrum and some dips were also present on the residuals. We added three Gaussian absorption components (`gabs`). From the model, the absorption features were obtained at 1.078 keV, 1.75 keV and 1.85 keV which correspond to the absorption lines of Fe XXII, Fe XXIII and Si XII respectively. The combined model gave the reduced  $\chi^2=1.34$  for 2596 degrees of freedom. After fitting three absorption components in the model, there was some emission like features in the residual near  $\sim 1.5$  keV and  $\sim 1.8$  keV. We added two Gaussian emission components at these specific positions. The Gaussian lines were obtained at 1.5 keV and 1.81 keV and after the introduction of these two emission lines, the fitting improved significantly with reduced  $\chi^2=0.88$  for 2592 degrees of freedom. The emission lines at 1.5 keV and 1.81 keV corresponds to Fe XXI and Fe XXIII emission lines respectively.

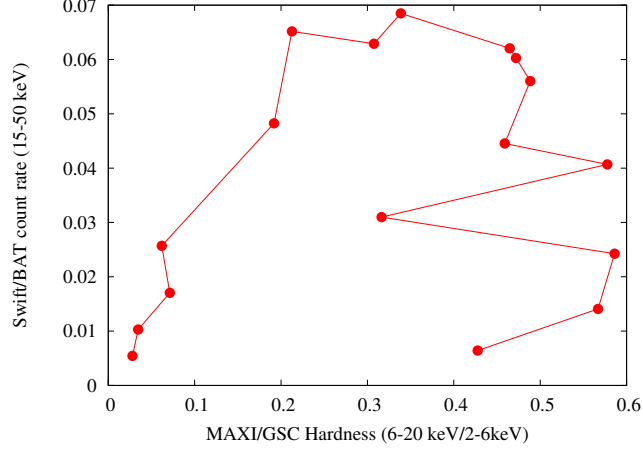


Fig. 5.— Hardness-Intensity diagram of black hole MAXI J1348–630 during the outburst of April using daily monitoring data of MAXI/GSC and Swift/BAT. The intensity has been plotted using the flux as measured by Swift/BAT in the energy range 15–50 keV and the corresponding hardness is plotted using the ratio of photon counts in 6–20 keV and 2–6 keV energy bands of MAXI/GSC. The figure shows the evolution of the source through different spectral states during the outburst.

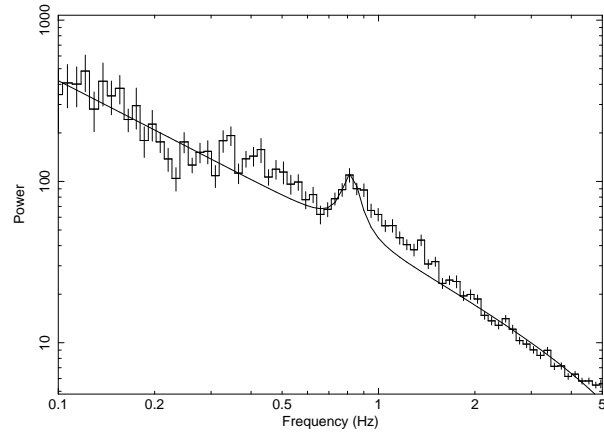


Fig. 6.— Power density spectrum of the source during the outburst of June using NICER observation with 0.1 s bin size. The presence of a low-frequency QPO at 0.82 Hz is detected with a Q-value of 6.86 and an RMS value of 7.6 per cent. The PDS is fitted with the combined model of constant, power-law and a Lorentzian component.

The spectrum in the energy range 2.3–6 keV was shown in the right of Figure 7. Since this spectrum was dominated by blackbody radiation from the accretion disk, we fitted it with a `bbbody` model. In this spectrum, multiple absorption features were evident from the residual as well as the spectrum also. We added three Gaussian absorption components at 2.73 keV, 3.22 keV and 3.32 keV which correspond to absorption lines of Cl XVI, S XV and Ar XVIII respectively. The reduced  $\chi^2$  value for the combined model was 1.38 for 1319 degrees of freedom. There was a clear hump-like feature near 3.6 keV observed from the residuals. To compensate for this, we added a Gaussian emission component at that position. As a result, the reduced  $\chi^2$  changed to 1.003 for 1317 degrees of freedom. This Gaussian emission line at 3.6 keV corresponds to the emission line of Ar XVI. All absorption and emission features were identified from the online spectral plotting facility of AtomDB<sup>5</sup>.

### 3.6. Evolution of spectral parameters

Spectra of the source MAXI J1348–630 were studied using NuSTAR/FPMA data that were collected over three epochs during the decaying phase of the June 2019 outburst. During these three observations, the source remained in the HS. Spectra were plotted in the energy range 3–78 keV. We studied the variation of spectral parameters by fitting all NuSTAR spectra from different observations. The spectra were fitted with a photoelectric absorption model `tbabs` (Wilms, Allen & McCray 2000) with a thermal Comptonisation component (`nthcomp`; Zdziarski, Johnson & Magdziarz (1996); Życki, Done & Smith (1999)) for the Comptonised hard photons. We added a blackbody component to take into account the blackbody emission from the accretion disk. By fitting with this model the value of reduced  $\chi^2$  was 1.23 for 1869 degrees of freedom with a clear hump near 6.4 keV in the residual indicating the Fe-K $\alpha$  emission line. The fit statistics enhanced significantly on adding a Gaussian component at 6.4 keV. Earlier, we fitted the spectra with a broken power-law instead of `nthcomp` in the above-said model. The fit statistic was not good enough and the model failed to resolve the Fe-K $\alpha$  line in each spectrum. The iron emission line at 6.4 keV was resolved from each spectrum after using the `nthcomp` model. Figure 8 showed the spectrum with the best-fitted model and the residuals of the source using NuSTAR/FPMA data (Obs Id – 80502304006) that gave reduced  $\chi^2 = 1.09$  for 1867 degrees of freedom. Evolution of spectral parameters over the outburst were shown in Table 4. During the fitting of the NuSTAR spectra, we fixed the value of hydrogen column density ( $n_H$ ) at  $0.86 \times 10^{22}$  cm $^{-2}$ , previously determined by Tominaga et al. (2020) from the Swift/XRT spectrum (1–10 keV).

---

<sup>5</sup><http://www.atomdb.org/Webguide/webguide.php>

Table 2: Chandra/HETG spectrum in the energy range 1–2 keV. The spectrum is fitted with the model  $\text{phabs} \times \text{gabs} \times \text{gabs} \times \text{gabs} \times (\text{powerlaw} + \text{gaussian} + \text{gaussian})$ . Values of each model parameter are shown below. Several absorptions and emission lines were detected from the spectrum which is mentioned in the table.

Model	Parameter	Value	Line ID
phabs	$n_H$ ( $10^{22}$ cm $^{-2}$ )	$1.19 \pm 0.01$	–
	$E_{gabs}$ (keV)	1.078	Fe XXII
gabs	$\sigma_{gabs}$ (keV)	$0.0065 \pm 0.0007$	–
	$E_{gabs}$ (keV)	1.75	Fe XXIII
gabs	$\sigma_{gabs}$ (keV)	$0.0196 \pm 0.0006$	–
	$E_{gabs}$ (keV)	1.85	Si XII
gabs	$\sigma_{gabs}$ (keV)	$0.017 \pm 0.001$	–
gaussian	$E_{gaussian}$ (keV)	1.5	Fe XXI
	$\sigma_{gaussian}$ (keV)	$0.20 \pm 0.02$	–
gaussian	$E_{gaussian}$ (keV)	1.81	Fe XXIII
	$\sigma_{gaussian}$ (keV)	$0.032 \pm 0.005$	–
$\chi^2_{reduced}$ (d.o.f.)		0.88 (2592)	

Table 3: The same Chandra/HETG spectrum in the energy range 2.3–6 keV. The best fitted model is  $\text{gabs} \times \text{gabs} \times \text{gabs} \times (\text{bbody} + \text{gaussian})$ . The corresponding absorption and emission lines are summarized in the table.

Model	Parameter	Value	Line ID
gabs	$E_{gabs}$ (keV)	2.73	Cl XVI
	$\sigma_{gabs}$ (keV)	$0.020 \pm 0.005$	–
gabs	$E_{gabs}$ (keV)	3.22	S XV
	$\sigma_{gabs}$ (keV)	$0.019 \pm 0.003$	–
gabs	$E_{gabs}$ (keV)	3.32	Ar XVIII
	$\sigma_{gabs}$ (keV)	$0.034 \pm 0.003$	–
gaussian	$E_{gaussian}$ (keV)	3.6	Ar XVI
	$\sigma_{gaussian}$ (keV)	$1.45 \pm 0.12$	–
bbody	kT (keV)	$1.24 \pm 0.06$	–
	Norm	$0.75 \pm 0.12$	–
$\chi^2_{reduced}$ (d.o.f.)		1.00 (1317)	

Throughout the outburst of June 2019, the spectra were hard and sufficient photon was present at 78 keV which indicated the possibility of the presence of hard tails extending up to a few hundred keV. The photon index was almost constant ( $\Gamma \sim 1.59$ ) over three epochs of NuSTAR observations. The average temperature due to blackbody radiation was  $\sim 0.7$  keV. Previously, [Tominaga et al. \(2020\)](#) found the inner disk temperature was  $\sim 0.75$  keV during the canonical SS of January 2019 outburst. The spectra were mainly dominated by hard Comptonised photons during the outburst. On the first NuSTAR observation (on MJD 58655), the contribution of thermally Comptonised flux to the total flux ( $F_{nthc}/F_{tot}$ ) was  $\sim 70$  per cent which increased to 80 per cent on the third observation (on MJD 58672). But, the contribution of Comptonised flux to total flux on MJD 58660 was significantly less ( $\sim 53$  per cent) reason of which is unclear. The blackbody normalization also decreased during this period indicating the lowering of emission of disk photons. At the same time, the increase in electron temperature upscattered the seed photons, increasing their energies beyond the energy of typical seed photons. As a result, the majority of seed photons were getting upscattered by inverse Comptonisation and dominated the spectra. Total flux also decreased as the observations were performed on the decaying phase of the outburst.

### 3.7. Continuum Image of MAXI J1348–630 using ALMA

We detected the continuum emission from black hole MAXI J1348–630 between the frequency range of 89.56–351.44 GHz with ALMA band 3, 4, 6 and 7 observations. The measured disk average flux densities in different frequencies varies between 12.18 to 18.47 mJy. The continuum images at different frequencies of MAXI J1348–630 were shown in Figure 1. The phase center of the continuum image of MAXI J1348–630 was RA=13h48m12.790s, Dec=−63°16'28.480" (J2000). In continuum images, the beam sizes were  $1.22'' \times 0.97''$  for 104 GHz,  $1.22'' \times 0.97''$  for 138 GHz,  $0.58'' \times 0.44''$  for 242 GHz, and  $0.35'' \times 0.29''$  for 343 GHz. The source was not resolved in any of the images indicating size of the radio emitting region was less than  $0.29''$ .

Table 4: Evolution of spectral parameters on different days of the June 2019 outburst as observed by NuSTAR/FPMA in the energy range 3–78 keV. The spectra were well fitted with an absorbed thermal Comptonisation model and blackbody radiation with a Gaussian component.

Day (MJD)	$\Gamma$	$kT_e$ (keV)	$kT_{bb}$ (keV)	Norm <sub>bb</sub>	$F_{tot}$ (erg cm $^{-2}$ s $^{-1}$ )	$F_{nthc}/F_{tot}$	$E_{gaussian}$ (keV)	$\sigma_{gaussian}$ (keV)	$\chi^2_{red}$ (d.o.f.)
58655	$1.591 \pm 0.002$	$18.4 \pm 0.3$	$0.70 \pm 0.01$	$0.0137 \pm 0.0004$	$2.127 \times 10^{-8}$	0.70	6.4	$1.35 \pm 0.04$	1.55 (1867)
58660	$1.590 \pm 0.002$	$21.2 \pm 0.4$	$0.72 \pm 0.01$	$0.0095 \pm 0.0003$	$1.899 \times 10^{-8}$	0.53	6.4	$1.07 \pm 0.05$	1.18 (1867)
58672	$1.586 \pm 0.002$	$23.5 \pm 0.6$	$0.68 \pm 0.01$	$0.0069 \pm 0.0003$	$1.293 \times 10^{-8}$	0.82	6.4	$1.13 \pm 0.06$	1.09 (1867)

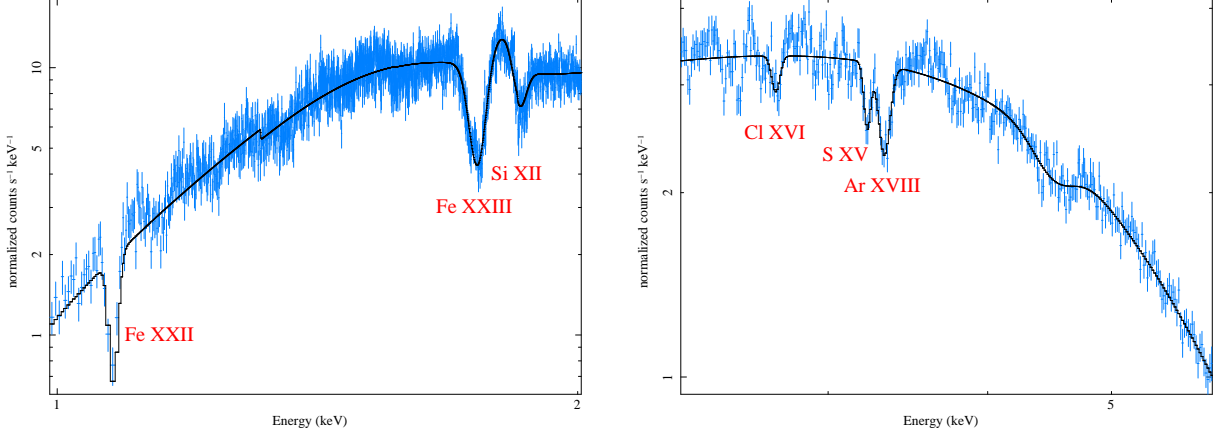


Fig. 7.— Chandra/HETG spectrum of MAXI J1348–630 during the outburst of June. The spectrum was studied using the observation of 21 June 2019 (Obs Id – 21239). The spectrum was divided into two different energy ranges to better study the emission and absorption features. The left figure showed the spectrum along with the fitted model in the energy range 1–2 keV whereas the right figure shows the same in 2.3–6 keV. Multiple Gaussian emission and absorption lines are detected from the model fitting of both spectra and the corresponding lines are listed in Table 2 and 3.

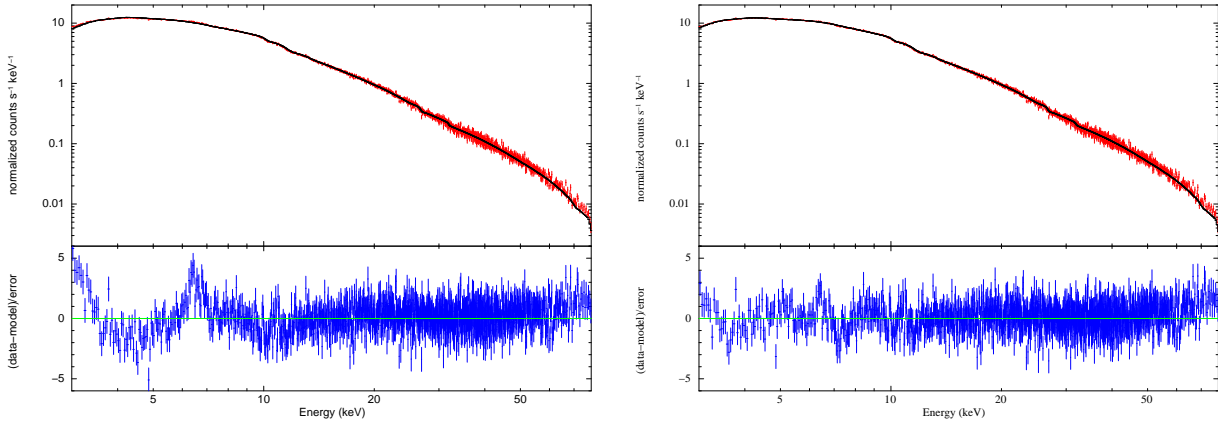


Fig. 8.— The spectra of the source in the energy range 3–78 keV using NuSTAR/FPMA data (Obs Id – 80502304006) and well fitted with a combined model of  $\text{tbabs} \times (\text{nthcomp} + \text{bbody} + \text{gaussian})$  with reduced  $\chi^2 = 1.09$  for 1867 degrees of freedom. The left figure was fitted with the above-said model but without the Gaussian component and a clear peak is visible in the residue near 6.4 keV. To compensate this feature, we added a gaussian component at 6.4 keV and the enhanced residual is shown in the right figure.

The resultant radio continuum spectrum of black hole MAXI J1348–630 was shown in Figure 9. The continuum radio spectrum showed the flat nature with spectral index ( $\alpha$ ) =  $0.324 \pm 0.003$  (assuming  $F_\nu \propto \nu^\alpha$ ). The slope of the spectrum was positive in the radio region, indicating that the synchrotron radiation was from an optically thick region and the self-absorption frequency was more than 351.4 GHz. The ALMA measurements were included in the broadband spectrum of Figure 10.

We looked for molecular line emission from the surrounding of the source, as was earlier found for the case of Galactic black holes GRS 1758–258 and 1E 1740.7–2942 (Tetarenko et al. 2020). No molecular lines were detected indicating that there was not enough molecular gas in the vicinity of MAXI J1348–630.

### 3.8. Broadband spectrum

We presented here a Spectral Energy Distribution (SED) over a multi-wavelength region of the black hole MAXI J1348–630 to get an overall idea about the emission mechanism from different emitting regions. The broadband SED was studied in a wide range of energy from radio to X-ray including ultraviolet and optical wavebands during the outburst of April 2019. In Figure 10, we showed the broadband spectrum of the source using close-simultaneous observations. All observations were made between 2 and 3 May of 2019 when the source was close to the peak of the outburst of April 2019. The ALMA observation was started at 03:06 UT on 2 May 2019 (MJD 58605.13) from which the radio emission from the compact jets was studied using different wavebands (band 3, 4, 6 and 7) with frequencies ranging from 89.56 GHz to 351.44 GHz. Swift observations corresponding to 3 May 2019 (MJD 58606) was used. Fluxes in the Ultraviolet region were taken from the UVOT observations performed on 3 May 2019. UVOT observations were carried out with *uvw2* and *uvm2* filters having central wavelength ( $\lambda$ ) of 1928 Å and 2246 Å respectively. The X-ray flux in 0.9–9 keV was included using data of XRT onboard Swift.

The optical flux was included from Swift/UVOT data that was performed with the *u* filter ( $\lambda = 3465$  Å) on 9 May 2019 for reference. We also indicated another optical photometry from Gaia DR2 catalogue (Brown et al. 2018) in the plot for comparison. The source remained undetected through UVOT observations of *u*, *uvm2* and *uvw2* bands and we mentioned  $5\sigma$  upper limits of the source. The flux measured by the Gaia catalogue (Brown et al. 2018) remained below these upper limits and was consistent with our study.

The broadband spectrum was studied when the source was in the intermediate state, making a transition from SS to HS, near the peak of the April 2019 outburst during the

decay phase. The source was strong in X-ray indicating strong blackbody radiation from the disk. In the region of radio wavelength, the spectrum was flat. Fitting the ALMA spectrum, we obtained  $\alpha = 0.324 \pm 0.003$  (assuming  $F_\nu \propto \nu^\alpha$ ) as measured on 2 May 2019. The low radio emission from jets indicated weak synchrotron emission from an optically thick regime. The low radio flux from MAXI J1348–630 categorized itself as “radio-quite” micro-quasar.

Due to the lack of sufficient photons in the mid-energy region, we did not fit the whole spectrum. But the X-ray spectrum in the range 0.9–8 keV is well described separately with the best-fitted model using the Swift/XRT observation of 3 May 2019 (MJD 58606.39). The model constituted a photo-electric absorbed power-law with a spectral index of 2.2. The emission of soft X-ray photons was dominated by thermal blackbody radiation from the innermost region of the accretion disk with a disk temperature of  $0.27 \pm 0.02$  keV.

The averaged X-ray flux during the April outburst was  $2.94 \times 10^{-9}$  erg cm $^{-2}$  s $^{-1}$  in 0.9–8 keV on MJD 58606.39. The quasi-simultaneous radio fluxes were 12.18–18.47 mJy (or  $1.18 \times 10^{-14}$  –  $6.46 \times 10^{-14}$  erg cm $^{-2}$  s $^{-1}$ ) as measured by ALMA band-3, 4, 6 and 7 at frequencies ranging between 97–350 GHz on MJD 58605.13–58605.19.

We have compared our result with results of [Carotenuto et al. \(2019\)](#) and [Chauhan et al. \(2019\)](#) which were studied during the outburst of January 2019. On MJD 58523.21, the radio flux at 1.28 GHz was  $520.3 \pm 5.0$  mJy or  $6.67 \times 10^{-15}$  erg cm $^{-2}$  s $^{-1}$  as observed by MeerKAT ([Carotenuto et al. 2019](#)). In another radio observation by Murchison Widefield Array (MWA) telescope on MJD 58523.79, fluxes at 154 MHz and 216 MHz were  $301 \pm 21$  mJy ( $4.64 \times 10^{-16}$  erg cm $^{-2}$  s $^{-1}$ ) and  $362 \pm 22$  mJy ( $7.82 \times 10^{-16}$  erg cm $^{-2}$  s $^{-1}$ ) respectively ([Chauhan et al. 2019](#)). The quasi-simultaneous X-ray flux on MJD 58523.44 by Swift/XRT (Obs Id – 00011107006) in the energy range 1–10 keV was  $1 \times 10^{-8}$  erg cm $^{-2}$  s $^{-1}$ . Although the source was bright in radio and X-ray bands, the radio flux compared to X-ray flux was significantly less during the January 2019 outburst which is observed during the outburst of April 2019 also.

#### 4. Discussions

In this work, we studied multi-wavelength observations of the black hole MAXI J1348–630 using ALMA, Chandra, NICER, Swift and NuSTAR during its two successive outbursts in April and June 2019.

Earlier, the source went to SS near MJD 58530 during the outburst of January 2019 and remained in that state until MJD 58597 ([Tominaga et al. 2020](#); [Zhang et al. 2020](#)). After remaining in the SS for approximately 67 days, it evolved through the intermediate states

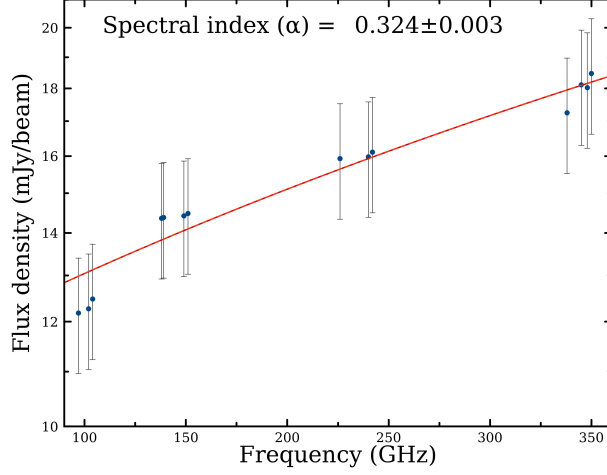


Fig. 9.— Radio continuum spectrum of MAXI J1348–630 between the frequency range of 89.56–351.44 GHz with the variation of flux density between 12.18–18.47 mJy. The continuum radio spectrum shows the flat nature with spectral index ( $\alpha$ ) =  $0.324 \pm 0.003$  (assuming  $F_\nu \propto \nu^\alpha$ ). The red color line indicated the best fitting single power low to determine the global spectral index from the continuum spectra.

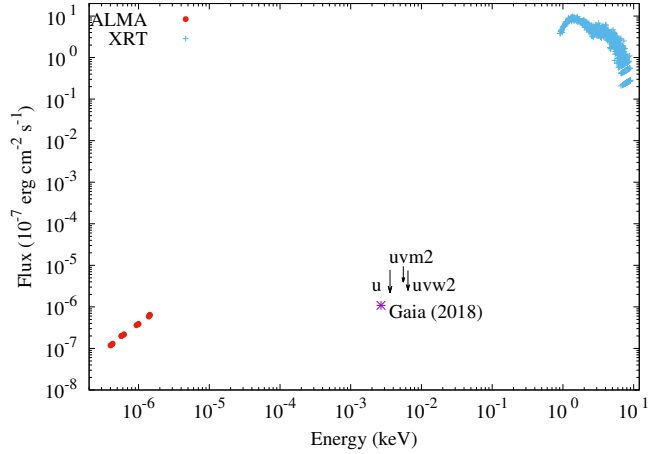


Fig. 10.— Broadband spectrum of the source MAXI J1348–630 from radio to X-ray band. The millimetre radio flux has been taken by analysing ALMA data which is shown by red circles. Ultraviolet and X-ray fluxes are included from UVOT and XRT data onboard the Swift observatory. The upper limit of the ultraviolet flux is denoted by a down arrow. The X-ray flux is shown by the blue points at the top right corner. The optical photometry has been taken from the Gaia DR2 catalogue, indicated by violet asterisk (Brown et al. 2018).

and reached the HS at the end of the outburst. The transition from SS to HS started when the luminosity of the source was about 7.3 per cent of the peak luminosity of the outburst of January 2019. During the June 2019 outburst, the source remained in the canonical HS throughout the outburst (Zhang et al. 2020). Similar re-brightening was also observed in another new X-ray transient MAXI J1820+070 and during the re-outburst, it also did not show any state transition (Stiele & Kong 2020). During the outburst of June of MAXI J1348–630, the peak luminosity was  $1.89 \times 10^{37}$  erg s $^{-1}$  (assuming the source distance to be 4 kpc according to Tominaga et al. (2020)), which is 13.6 per cent the peak luminosity of the January 2019 outburst.

The accretion mechanism around a BHXR is still not understood properly. Multi-wavelength observations are key to understand the emission mechanisms from different regions of BHXR during outbursts (viz. Ueda et al. (2002); Chakrabarti et al. (2005)). While the sources of X-ray and radio wavelength radiation are well understood, the origin of mid-energy emissions in the infra-red, ultraviolet and visible wavebands are rather complicated to understand (van Paradijs & McClintock 1995; Chakrabarti, Pal & Nandi 2006), since multiple radiation mechanisms occur at different regions of the system. The soft X-rays are believed to come from the inner-most regions of the accretion disk, whereas the ultraviolet and optical emissions are thought to come from the irradiated outer thin accretion disks (Poutanen & Veledina 2014). Origin of the hard X-rays may be due to inverse Comptonisation of the disk photons by the electron clouds around the black hole called “Corona” (Done et al. 2007). Radio emissions are originated due to Synchrotron emission from the jets (Falcke & Biermann 1996, 1999).

In this multi-wavelength study, we observed that the emission of the X-ray from the disk is much stronger than the emission in the radio wavelength. This implies that the emission from the source is dominated by the blackbody radiation from the accretion disk associated with weak synchrotron emission from the optically thick regime around the compact jets. Mis-aligned jets may be the reason for low radio luminosity (Miller-Jones et al. 2019). Self-absorption frequency was more than 351.4 GHz as observed from the radio observations.

The emission in the mid energy region, i.e., in the ultraviolet and optical wavelength was significantly less as usually observed in X-ray binaries. This was probably due to the heavy extinction as dust and matters are accumulated around the system (Zwitter, Calvani & D’Odotico 1991; Paragi et al. 1999). Earlier, some multi-wavelength observations were performed in other sources to study the accretion phenomenon around them. The same nature of radio weak and X-ray strong, as observed in MAXI J1348–630 during April 2019 outburst, were also observed in GRS 1915+105 (Ueda et al. 2002), GX 339–4 (Cadolle et al. 2011) etc. In the study of a multi-wavelength campaign (April 2002) of the micro-quasar GRS 1915+105,

[Ueda et al. \(2002\)](#) found that radio emissions from jets were relatively weak whereas the X-rays emitted from the disk were much stronger. The same nature of SED was observed in the LMXB GX 339–4 during the outburst of 2010 ([Cadolle et al. 2011](#)). But during the broadband study of the HMXB SS 433, [Chakrabarti et al. \(2005\)](#) noticed that source is remarkably strong in radio wavelength but with the increase in energy, the flux was drastically decreasing in the infra-red, optical, ultraviolet region and significantly less in X-ray.

BHXRBS show variabilities on different time scales. In BHXRBS, different types of QPOs are present in the PDS associated with some noise components in different phases of the outburst ([Casella, Belloni & Stella 2005; Motta 2016](#)). Type-A QPOs are relatively rare to observe in BHXRBS. They appear with broader and flat peaks in 4–8 Hz and typically observed in the SS, when the variability reaches the minimum (fractional RMS of few per cent) ([Homan et al. 2001](#)). Since the fundamental peak itself is weak and appear with a wide range of frequency, harmonics are not generally observed. Type-B QPOs are found during the SIMS of an outburst. They usually appear with sharp peaks and narrow widths and found at around 6 Hz ([Casella et al. 2004; Motta et al. 2011; Sriram, Rao & Choi 2013; Motta 2016; Stevans & Uttley 2016](#)). Harmonics and sub-harmonics are often present in the PDS. The most common type of QPOs observed in BHXRBS are Type C QPOs. They are also observed with strong peak and narrow width typically found within a few mHz to 30 Hz ([Casella et al. 2004; Motta et al. 2011; Motta 2016](#)). They are observed in the HS and HIMS, generally appears with harmonic and sub-harmonics in the PDS.

In our study, we found the PDS was characterized by strong band-limited noise with RMS variability of  $31.4 \pm 0.5$  per cent on MJD 58654 which is typically found in the HS of a BHXR. The decrease in QPO frequency, RMS and quality factors are quite common in the decaying phase of the outburst of a BHXR. Positions of the QPOs, RMS and quality factor suggested that those were similar to type-C QPOs, typically observed in the HS of an accreting BHXR ([Motta 2016](#)). Type C QPOs were also observed previously from this source at different frequencies during the outburst of January 2019 ([Jana et al. 2020; Zhang et al. 2020](#)). The variation in QPO frequency indicated a certain change in oscillation near the Comptonising regions ([Chakrabarti, Acharyya & Molteni 2004](#)) or may be due to the change in perturbation inside the Keplerian disk ([Trudolyubov, Churazov & Gilfanov 1999](#)). The origin of QPOs from BHXRBS is still a subject of debate. Multiple models are proposed to explain the origin of type-C QPOs. They are believed to originate due to relativistic precession of the inner-most regions of a cool and optically thick truncated disk ([Shakura & Sunyaev 1973; Ingram, Done & Fragile 2009](#)) or due to instabilities of accretion disks around the compact object as a result of magneto-acoustic oscillation ([Titarchuk & Fiorito 2004](#)).

In the HS of BHXRBS, the energy spectra are strongly dominated by Comptonised emis-

sion with a weak and cool thermal component emitted from truncated disks (Done et al. 2007). Whereas in SS, emissions are characterized by strong thermal blackbody radiation from the disk and the effect of Comptonisation becomes minimum. During this state, the inner disk radius sometimes extends up to the innermost stable circular orbit (Tanaka 1989; Ebisawa et al. 1993; Steiner et al. 2010). The energy spectra are almost equally dominated by both blackbody and Comptonisation components during the intermediate states. During the transition towards harder states, the Comptonisation component starts dominating the spectra and fluxes are mostly due to the hard photons (Takahashi et al. 2008; Makishima et al. 2008). During the NuSTAR observations, the source remained entirely in the HS and the energy spectra were strongly dominated by the thermal Comptonisation component as observed from the study of the spectral evolution. Over three epochs of NuSTAR observations, when the source moved towards the quiescence, the flux of Comptonised photons increased indicating the spectral hardening nature.

During the HS, the spectral index ( $\Gamma$ ) remained almost constant at  $\sim 1.6$ . The corresponding blackbody temperature also remained almost constant at  $\sim 0.7$  keV which was comparatively small when the luminosity was near to the maximum (in the order of  $10^{37}$  erg s $^{-1}$ ) during the outburst of June 2019. The luminosity of the source depends on the temperature and radius of the source as  $L \propto R^2 T^4$ . According to the equation, a cool disk and high luminosity indicate a relatively larger disk radius. The large radius suggests that the source is massive compared to most of the known Galactic black holes. Also, the temperature of a standard accretion disk is inversely proportional to the black hole mass,  $T \propto M^{-1/4}$  (Shakura & Sunyaev 1973; Zhang et al. 2020). During the NuSTAR observations, the lower disk temperature of the source indicated that the system may hosts a relatively high mass black hole as stated earlier by Tominaga et al. (2020) and Jana et al. (2020).

## 5. Conclusion

We summarized the result of different timing and spectral properties of the X-ray binary black hole MAXI J1348–630 during its two consecutive outbursts of April and June 2019 occurred between MJD 58596 and MJD 58710. A study of hardness evolution showed the hardness ratio was rapidly varying during the outburst of April 2019 indicating a state transition from SS to HS and the hardness ratio remained almost constant during the outburst of June 2019. The power density spectra were dominated by strong band-limited noise components with typical RMS variability of  $\sim 30$  per cent. Type-C QPO of  $6.83\sigma$  was detected on MJD 58654 using NICER data (0.2–12 keV) at frequency 0.82 Hz with 7.6 per cent RMS amplitude. Another QPO of  $5.58\sigma$  was detected on MJD 58655 from NuSTAR

data (3–80 keV) at 0.67 Hz with an RMS amplitude of 2.1 per cent. A rapid decrease in RMS indicated a certain geometrical change in corona. We measured the improved source location at RA=13h48m12.883s, Dec=−63°16'28.82" (J2000) using Chandra HETG observation. We studied the broadband spectrum of the black hole using the fluxes in radio, optical, ultraviolet and X-ray energy bands during the outburst of April 2019 to understand the emission from different regions of the system at different wavelengths. The broadband spectrum suggested that the disk emission was much stronger than the emission from the jets. Heavy extinction in the optical/UV region was observed. This was probably due to the presence of matter or dust that were accumulated around the system. Chandra/HETG spectrum was studied from which multiple broad Gaussian absorption lines and some weak emission lines were detected. The evolution of spectral parameters was also studied using three different observations of NuSTAR during the June 2019 outburst. The best fit model suggested that the spectra were mainly dominated by the thermally Comptonised photons as usually observed in the HS of a BHXR. Signature of iron  $K_{\alpha}$  emission lines were detected from all three NuSTAR spectra.

### Acknowledgements

This research has made use of data and/or software provided by the High Energy Astrophysics Science Archive Research Center (HEASARC), which is a service of the Astrophysics Science Division at NASA/GSFC. We have also used **CIAO**, developed by the Chandra X-ray Observatory team. The scientific results reported in this article, especially the high-resolution spectrum and source localization are based on data obtained from the Chandra Data Archive. **NUSTARDAS** tools by ESA and Caltech played important roles in this research. This research has made use of **SAOImage DS9**, developed by the Smithsonian Astrophysical Observatory. Data products that have been used in this research are collected from HEASARC data archives. Special thanks to Neil Gehrels Swift Observatory and MAXI-RIKEN teams since daily monitoring data of Swift/BAT and MAXI/GSC have been used in this research.

This paper makes use of the following ALMA data: ADS /JAO.ALMA#2016.1.01235.S. ALMA is a partnership of ESO (representing its member states), NSF (USA) and NINS (Japan), together with NRC (Canada), MOST and ASIAA (Taiwan), and KASI (Republic of Korea), in cooperation with the Republic of Chile. The Joint ALMA Observatory is operated by ESO, AUI/NRAO and NAOJ.

## 6. Data Availability

Data used in this work are available in the HEASARC browse portal provided by High Energy Astrophysics Science Archive Research Center (HEASARC) at <https://heasarc.gsfc.nasa.gov/cgi-bin>. The data that support the plots within this paper and other findings of this study are available from the corresponding author upon reasonable request. The raw ALMA data are publicly available at <https://almascience.nao.ac.jp/asax/> (project id: 2018.1.01034.T).

## REFERENCES

Alpar M. A., Shaham J., 1985, *Nature*, 316, 239

Arnaud K. A., 1996, in Jacoby G. H., Barnes J., eds, *ASP Conf. Ser. Vol. 101, Astronomical Data Analysis Software and Systems V*. Astron. Soc. Pac., San Francisco, p. 17

Barthelmy S. D., et al., 2005, *SSRv*, 120, 143B

Belloni T. M., 2009, *Lecture Notes in Physics*, 794, 53

Belloni T. M., Zhang L., Kylafis N. D., Reig P., Altamirano, D., 2020, *MNRAS*, 496, 4366B

Belloni T. M., Motta S. E., Muñoz-Darias T., 2011, *BASI*, 39, 409B

Brinkman A. C., et al., 2000, *ApJ*, 530, L111

Brown A. G. A., et al., 2018, *A&A*, 616A, 1G

Burrows D. N., et al., 2000, *SPIE*, 4140, 64B

Cadolle B. M., et al., 2011, *A&A*, 534, 119C

Canizares C. R., et al., 2005, *PASP*, 117, 1144

Carotenuto F., Tremou E., Corbel S., Fender R., Woudt P., Miller-Jones J., 2019, *The Astronomer's Telegram*, 12497, 1

Carotenuto F., et al., 2021, *MNRAS*, tmpL, 51C

Casella P., Belloni T., Homan J., Stella L., 2004, *A&A*, 426, 587

Casella P., Belloni T., Stella L., 2005, *ApJ*, 629, 403

Charles P. A., Coe M. J., 2006, *csxs.book*, 39, 215

Chakrabarti S. K., Acharyya K., Molteni D., 2004, A&A, 421, 1

Chakrabarti S. K., et al., 2005, MNRAS, 362, 957C

Chakrabarti S. K., Pal S., Nandi A., 2006, A&A, 453, 965C

Chauhan J., et al., 2021, MNRAS, 501L, 60C

Chauhan J., Miller-Jones J., Anderson G., Russell T., Hancock P., Bahramian A., Duchesne S., Williams A., 2019, The Astronomer’s Telegram, 12520, 1

Corbel S., Nowak M. A., Fender R. P., Tzioumis A. K., Markoff S., 2003, A&A, 400, 1007

Denisenko D., et al., 2019, The Astronomer’s Telegram, 12430, 1

Done C., Gierliński M., Kubota A., 2007, A&ARv, 15, 1

Dunn R. J. H., et al., 2010, MNRAS, 403, 61

Ebisawa K., et al., 1993, ApJ, 403, 684

Falcke H., Biermann P. L., 1996, A&A, 308, 321

Falcke H., Biermann P. L., 1999, A&A, 342, 49

Fender R., 2006, Jets from X-ray binaries (Compact stellar X-ray sources), 381, 419

Gallimore J. F., Baum S. A., O’Dea C. P., Pedlar A., Brinks E., 1999, ApJ, 524, 684

Gallo E., 2010, Lecture Notes in Physics, Berlin Springer Verlag, 794, 85

Gallo E., Fender R. P., Pooley G. G., 2003, MNRAS, 344, 60

Gendreau K. C., et al., 2016, in Proc. SPIE. p. 99051H, doi:10.1117/12.2231304

Gurzadian V. G., Ozernoi L. M., 1979, Nature, 280, 214G

Harrison F. A., et al., 2013, ApJ, 770, 103

Homan J., Belloni T., 2005, Ap&SS, 300, 107

Homan J., Wijnands R., van der Klis M., Belloni T., van Paradijs J., Klein-Wolt M., Fender R., Méndez M., 2001, ApJS, 132, 377

Ingram A., Done C., Fragile P. C., 2009, MNRAS, 397, L101

Jana A., Debnath D., Chatterjee D., Chakrabarti S. K., Chatterjee K., Bhowmick R., 2019, The Astronomer’s Telegram, 12505, 1

Jana A., Debnath D., Chatterjee D., Chatterjee K., Chakrabarti S. K., Naik S., Bhowmick R., Kumari N., 2020, *ApJ*, 897, 3

Kennea J. A., Negoro H., 2019, The Astronomer’s Telegram, 12434, 1

Makishima K., et al., 2008, *PASJ*, 60, 585

Miller J. M., Raymond J., Reynolds C. S., Fabian A. C., Kallman T. R., Homan J., 2008, *ApJ*, 680, 1359

Miller-Jones J. C. A., et al., 2019, *Nature*, 569, 374

Motta S. E., 2016, *Astronomische Nachrichten*, 337, 398

Motta S., Muñoz-Darias T., Casella P., Belloni T., Homan J., 2011, *MNRAS*, 418, 2292

Negoro H., et al., 2019, The Astronomer’s Telegram, 12838, 1

Pal S., Chakrabarti S. K., Kraus A., Mandal S., 2006, *BASI*, 34, 1P

Paragi Z., Vermeulen R. C., Fejes I., Schilizzi R. T., Spencer R. E., Stirling A. M., 1999, *A&A*, 348, 910

Paul B., Rao A. R., 1998, *A&A*, 337, 815

Perley R. A., Butler B. J., 2017, *ApJ*, 230, 1538

Poole T. S., et al., 2008, *MNRAS*, 383, 627P

Poutanen J., Veledina A., 2014, *SSRv*, 183, 61

Remillard R. A., McClintock J. E., 2006, *ARA&A*, 44, 49

Sanna A., et al., 2019, The Astronomer’s Telegram, 12447, 1

Shakura N. I., Sunyaev R. A., 1973, *A&A*, 500, 33

Sreehari H., Ravishankar B. T., Iyer N., Agrawal V. K., Katoch T. B., Mandal S., Nandi A., 2019, *MNRAS*, 487, 928S

Sriram K., Rao A. R., Choi C. S., 2013, *ApJ*, 775, 28

Steiner J. F., et al., 2010, *ApJL*, 718, L117

Stevens A. L., Uttley P., 2016, MNRAS, 460, 2796

Stiele H., Kong A. K. H., 2020, ApJ, 889, 142

Takahashi H., et al., 2008, PASJ, 60, 69

Tanaka Y., 1989, in ESA Special Publication, Vol. 1, Two Topics in X-Ray Astronomy, Volume 1: X Ray Binaries. Volume 2: AGN and the X Ray Background, ed. J. Hunt & B. Battrick, 3

Tominaga M., et al., 2020, ApJ, 899, 20

Titarchuk L., Fiorito R., 2004, ApJ, 612, 988

Tetarenko A. J., Rosolowsky E. W., Miller-Jones J. C. A., Sivakoff G. R., 2020, MNRAS, 497, 3504

Trudolyubov S., Churazov E., Gilfanov M., 1999, A&A, 351, L15

Tsunemi H., Kitamoto S., Okamura S., Roussel-Dupre D., 1989, ApJ, 337, L81

Ueda Y., et al., 2002, ApJ, 571, 918

van der Klis M., 2006, Rapid X-ray Variability. pp 39–112

van der Klis M., Stella L., White N., Jansen F., Parmar A. N., 1987, ApJ, 316, 411

van Paradijs J., McClintock J. E. 1995, xrbi.nasa, 58

Wilms J., Allen A., McCray R., 2000, ApJ, 542, 914

Yadav J. S., 2001, ApJ, 548, 876Y

Yatake F., et al., 2019, The Astronomer’s Telegram, 12425, 1

Yusef-Zadeh F., et al., 2009, ApJ, 706, 348Y

Zhang L., et al., 2020, MNRAS, 499, 851Z

Zdziarski A. A., Johnson W. N., Magdziarz P., 1996, MNRAS, 283, 193Z

Zwitter T., Calvani M., D’Odorico S., 1991, A&A 251, 92

Życki P. T., Done C., Smith D. A., 1999, MNRAS, 309, 561Z